ACS Catalysis

Research Article

pubs.acs.org/acscatalysis

Efficient Oxygen Electroreduction: Hierarchical Porous Fe−N-doped Hollow Carbon Nanoshells

Yuan Wang,[†] Aiguo Kong,[‡] Xitong Chen,[‡] Qipu Lin,[‡] and Pingyun Feng*[,†,‡]

[†]Materials Science and Engineering Program and [‡]Department of Chemistry, University of California−Riverside, Riverside, California 92521, United States

Supporting Information

ABSTRACT: Hierarchical porous carbon nanoshells with about 40 nm cavities are synthesized by using CdS@mSiO$_2$ core−shell structured materials as hard templates and 4,4′-bipyridine and FeCl$_3$·6H$_2$O as nitrogen, carbon, and iron sources. CdS@mSiO$_2$ denotes a CdS nanoparticle core and mesoporous SiO$_2$ (mSiO$_2$) shell. The obtained porous and hollow carbon nanoshells demonstrate excellent electrocatalytic activity for oxygen reduction reaction (ORR). Both the onset potential (0.98 V) and half-wave potential (0.85 V) are more positive than that of commercial Pt/C in alkaline conditions with the same catalyst loading (0.1 mg cm^{-2}). In acidic conditions, the onset and half-wave potentials of carbon-nanoshell electrodes are only 30 and 20 mV less than that of commercial Pt/C, respectively. The outstanding stability and electrocatalytic activity for ORR of these novel carbon nanoshells can be attributed to the use of a Fe−N$_x$ containing precursor, hierarchical porous structural features, and perhaps most importantly the hollow shell design. Such hollow carbon nanoshells exhibit high performance as electrocatalysts for ORR; also this synthetic approach represents a versatile, new route toward the preparation of efficient materials with hierarchical porous and hollow structural features.

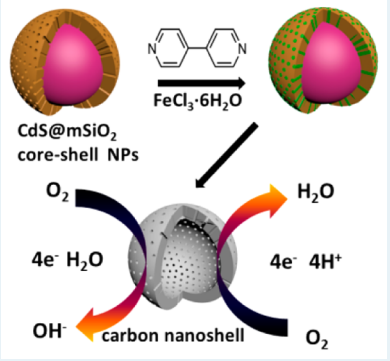

KEYWORDS: *carbon-nanoshell, nonprecious metal catalyst, porous structure, nanoparticles, oxygen reduction*

1. INTRODUCTION

The oxygen reduction reaction occurring at the cathode of proton exchange membrane fuel cells (PEMFCs) and metal−air batteries is a bottleneck reaction for the commercialization of these energy techniques. Currently, platinum and platinum-based alloys are the most efficient catalysts for the oxygen reduction reaction (ORR).[1] However, the high cost, scarcity, low tolerance to methanol fuel, and poor stability of Pt-based materials hinder the widespread utilization of these noble metal cathode catalysts. There are currently extensive efforts devoted to the development of nonprecious metal catalysts (NPMCs). Among the various catalysts, transition metal−nitrogen−carbon (Me−N−C) containing materials, especially Fe−N−C, have been demonstrated as a family of promising NMPCs for oxygen reduction reaction (ORR) due to their high ORR activity in both alkaline and acidic electrolytes.[2,3] However, the ORR activities of the present Fe−N−C materials are still less than that of Pt/C, especially in acidic conditions. The development of nonprecious metal catalyst with highly active ORR activity remains a challenge.

To construct highly active Fe−N*x* sites for ORR, in addition to introducing iron-containing active sites, the selection of other reaction precursors also plays a pivotal role in ORR activity and durability. Generally, three different nitrogen bonding environments exist in Fe−N−C catalysts: C≡N based nonaromatic bonds; C−N based nonaromatic bonds and N-containing aromatic bonds.[4] These can be obtained with different precursors. It is noticed that catalysts derived from aromatic precursors, such as polyaniline (PANI), exhibit a better combination of activity and durability than that of catalysts derived from nonaromatic precursors.[4] This is because heat treatments of aromatic precursors like aniline are believed to facilitate the incorporation of nitrogen containing active sites into the graphitized carbon matrix in the presence of iron and/or cobalt.[4,5] However, the nitrogen atoms in PANI are outside of the aromatic ring and thus have a great tendency of loss during high temperature heat treatments. It would be beneficial to have precursors with N-containing aromatic rings. Such a compound, 2,2′-bipyridine, has been reported to have good ORR properties.[6,7] Unlike 2,2′-bipyridine, 4,4′-bipyridine can form coordination compounds with extended structure through Fe and N bonding. Not investigated in the ORR field yet, it could have advantages of preventing the agglomeration during the heat treatment process and facilitating uniform distribution of active sites on the catalyst surface.[8]

In order to maximize the number of active sites, different templates, Ni foam, SBA 15, melamine foam, silica colloid, metal organic frameworks (MOFs) have been developed to prepare porous metal-containing nitrogen-doped carbon materials.[9−12] Among the various porous materials, hierarchical porous materials tend to provide more active sites and facilitate the transport and adsorption of oxygen.[6] Among numerous

Received: March 12, 2015
Revised: April 18, 2015
Published: April 20, 2015

DOI: 10.1021/acscatal.5b00530
ACS Catal. 2015, 5, 3887−3893

carbon-based electrode materials, hollow carbonaceous spheres have attracted attention due to the high surface-to-volume ratios and more accessible active sites on the shell.[13] The nanoshells act as release pathways and nanoreactors for encapsulated substances and outside species.[13] Nitrogen-doped hollow carbon spheres were investigated in the past few years and showed promising ORR properties.[13−18] However, hierarchical porous materials of small monodispersed sizes (<50 nm) with Fe−N−C hollow shells are rarely reported.

Here, we demonstrate a new design for the synthesis of Fe−N-doped hierarchical porous carbon hollow nanoshells employing core−shell CdS@mSiO$_2$ as templates. Cheap and abundant 4,4′-bipyridine and FeCl$_3$·6H$_2$O are chosen as carbon, nitrogen, and iron sources. The prepared hollow porous Fe−N−C catalysts possess uniform particle sizes less than 50 nm. The Fe−Nx active sites in the synthesized materials are homogeneously distributed on the surface, which has a Brunauer−Emmett−Teller (BET) surface area up to 1189 m^2/g with both microporosity and mesoporosity. These structural features together with an experimentally optimized graphitization process endow the materials with enhanced mass transfer efficiencies, large accessible pore volume, and good electrical conductivity. These characteristics are desirable for efficient electrocatalytic activity.

2. EXPERIMENTAL SECTION

2.1. Synthesis of CdS Nanoparticles.[19] A 3 mmol portion of sulfur powder, 3 mmol Cd(CH$_3$COO)$_2$·2H$_2$O, and 120 mL oleic acid (OA) were added to a 250 mL three-neck flask. The reaction mixture was heated to 285 °C for 4 h under argon flow. After cooling to room temperature, excess methanol was added with subsequent centrifugation and washing with ethanol for three times.

2.2. Synthesis of CdS@mSiO$_2$ Core−Shell Nanoparticles.[20] The CdS@mSiO$_2$ core−shell nanoparticles were prepared through a versatile sol−gel method. An 18 mg portion of CdS nanoparticles with oleic acid capping agent were dispersed in 3 mL chloroform. Then 300 mL 0.55 M aqueous ethyltrimethylammonium bromide (CTAB) solution was poured to the above solution and stirred vigorously for 30 min. The resulting oil-in-water microemulsion was then heated up to 60 °C and aged at that temperature for 10 min to evaporate chloroform under argon flow. Then 1.8 mL of 2 M NaOH solution was added to the mixture and heated to 70 °C in argon flow. After that, 18 mL ethyl acetate and 3 mL TEOS was added to the reaction solution in sequence and stirred for 3 h. After cooling, the resultant product was separated followed by washing with ethanol three times. Finally, the purified samples were redispersed in 300 mL acetone and refluxed at 80 °C for 48 h to remove the CTAB template.

2.3. Synthesis of Carbon Nanoshell. The carbon nanoshell was prepared through a nanocasting procedure. Typically, 10 mL water was added to a 15 mL ethanol solution containing 346 mg FeCl$_3$·6H$_2$O and 200 mg 4,4′-bipyridine with a molar ratio of FeCl$_3$·6H$_2$O to 4,4′-bipyridine was 1:1. After the solution became clear, 250 mg CdS@mSiO$_2$ core−shell nanoparticles were poured into the above solution and stirring vigorously overnight to evaporate the solvent at room temperature. Then the material was pyrolyzed at 900 °C in argon atmosphere for 3 h with a heating speed of 3°/min. Finally, the materials were etched with 5 wt % HF to remove CdS@mSiO$_2$ template. The carbon sheet was prepared by the same procedure but with no addition of CdS@mSiO$_2$ core−shell templates.

2.4. Electrocatalytic Activity Measurements. Electrochemical characterization of the catalysts was performed in a conventional three-electrode cell using CHI760D electrochemical workstation (CH Instruments, USA) controlled at room temperature and under atmospheric pressure. Ag/AgCl and platinum wire were used as reference and counter electrodes, respectively. All potentials in this report were converted into reversible hydrogen electrode (RHE).

A ring-disk electrode (RDE) with a glassy carbon disk and a Pt ring was served as the substrate for the working electrode. The catalyst ink was prepared by mixing the catalyst powder (10 mg) with 80 μL Nafion solution (5 wt %) and 1.2 mL ethanol in an ultrasonic bath. Then 2.5 μL of catalyst ink was pipetted onto the GC electrode with a catalyst loading of 0.1 mg cm^{-2} in 0.1 M KOH. In 0.1 M HClO4 solutions, 15 μL of catalyst ink was deposited onto the GC electrode corresponding a catalyst loading of 0.6 mg cm^{-2}. As a comparison, commercial 20 wt % platinum on Vulcan carbon black (Pt/C from Alfa Aesar) was prepared by blending Pt/C (10 mg) with 80 μL Nafion solution (5 wt %) and 1.2 mL ethanol in an ultrasonic bath. A Pt loading about 20 μg cm^{-2} was applied in both alkali and acid conditions.

Linear sweep voltammetry (LSV) polarization curves for the oxygen reduction reaction (ORR) were measured in an oxygen saturated 0.1 M KOH and 0.1 M HClO$_4$ electrolyte with a sweep rate of 10 mV s^{-1} at various rotating speeds from 400 to 2500 rpm. The cyclic voltammogram (CV) were recorded in solutions saturated with either Ar or O$_2$ gas without rotation with same sweep rate as that of LSV curve. The electron transfer number (n) and kinetic current density (j_K) were analyzed on the basis of Koutecky−Levich equations shown below:

$$1/j = 1/j_L + 1/j_K$$

$$j_L = 0.62nFCD^{2/3}\upsilon^{-1/6}w^{-1/2} = Bw^{-1/2}$$

$$1/j = 1/Bw^{-1/2} + 1/j_K$$

where $B = 0.62nFC_0D_0^{2/3}\upsilon^{-1/6}$, j was the measured current density, j_K and j_L were the kinetic- and diffusion-limiting current densities, w was the rotation speed, n was the electron transfer number, F was the Faraday constant (F = 96485 C mol^{-1}), C was the bulk concentration of O$_2$, D was the diffusion coefficient of dissolved oxygen, and υ was the kinematic viscosity of the electrolyte.

2.5. Characterization. The crystal structures of the materials were characterized by X-ray diffractometer (XRD) (D/Max2000, Rigaku) using a Bruker D8-Advance powder diffractometer operating at 40 kV, 40 mA for Cu Kα radiation (λ = 1.5406 Å). The morphology and composition of the samples were analyzed with a Tecnai T12 transmission electron microscope (TEM) and a Philips FEI XL30 field emission scanning electron microscope (FESEM) equipped with a LaB6 electron gun, and an EDAX energy-dispersive spectrometer (EDS). The surface properties and composition of the materials were studied by X-ray photoelectron spectroscopy (XPS) characterization using a Kratos AXIS ULTRADLD XPS system equipped with an Al K monochromated X-ray source and a 165 mm electron energy hemispherical analyzer. The shifts in energy (charging) of the XPS spectra were calibrated using the

DOI: 10.1021/acscatal.5b00530
ACS Catal. 2015, 5, 3887−3893

C 1s peak at 284.6 eV as a reference peak. Nitrogen sorption analysis was conducted at 77 K using a Micromeritics ASAP 2020 surface-area and pore-size analyzer. The specific surface areas were calculated using the Brunauer–Emmett–Teller (BET) equation from the nitrogen adsorption data in the relative range (P/P_0) of 0.04–0.20. The pore size distribution (PSD) plot was recorded from the adsorption and desorption branch of the isotherm based on the Barrett–Joyner–Halenda (BJH) and Horvath–Kawazoe (HK) model. The elemental analysis was performed by the Atlantic Microlab in Georgia.

3. RESULTS AND DISCUSSION

3.1. Catalyst Preparation and Characterization. The fabrication process of the carbon nanoshells is depicted in Scheme 1. First CdS nanoparticles with a size around 25 nm are

Scheme 1. Schematic Illustration of the Synthetic Process of Hierarchical Hollow Carbon Nanoshells

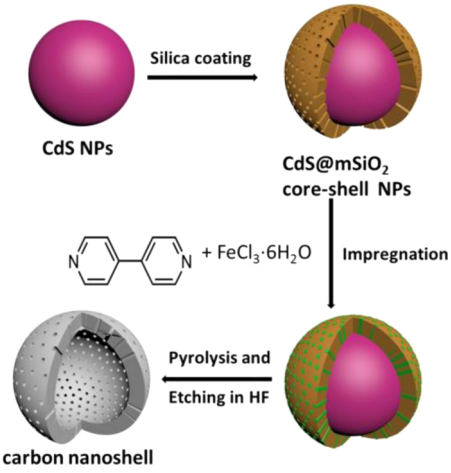

synthesized and serve as seeds for the synthesis of CdS@mSiO$_2$ core–shell nanoparticles.[20] The thickness of mesoporous silica shell can be tuned by the amount of silica precursors used and gelation temperatures. The precursors 4,4′-bipyridine and $FeCl_3{\cdot}6H_2O$ are first dissolved in water–ethanol solution and then the solution is mixed with CdS@mSiO$_2$ core–shell nanoparticles. The precursors are introduced into the mesoporous silica shell during the water and ethanol evaporation process. The obtained solid composites are then calcinated at 900 °C and subsequently treated with HF to remove the template. More experimental details can be found in the SI. All atoms on the aromatic ring structures of 4,4′-bipyridine possess sp2 hybridization which promotes the doping of nitrogen atoms in the graphitized carbon matrix at high temperature.[4] In addition, the surface pyridinic nitrogen coordinated with iron can lead to catalytically favorable active sites for ORR.[21,22]

Powder X-ray diffraction (XRD) patterns (Figure S2C) indicate that the synthesized carbon nanoshells are graphitic carbon with the (002) and (100) planes appearing at diffraction peaks of 26.1 and 43.2.[23] Figure 1a shows the typical transmission electron microscopy (TEM) images of the prepared CdS nanoparticles, and Figure 1b shows the corresponding CdS@mSiO$_2$ core–shell nanoparticles with 10 to 15 nm mesoporous silica shells (the porosity feature and surface area of CdS@mSiO$_2$ core–shell template are shown in Figure S5 and Table S3). After pyrolysis at 900 °C and the

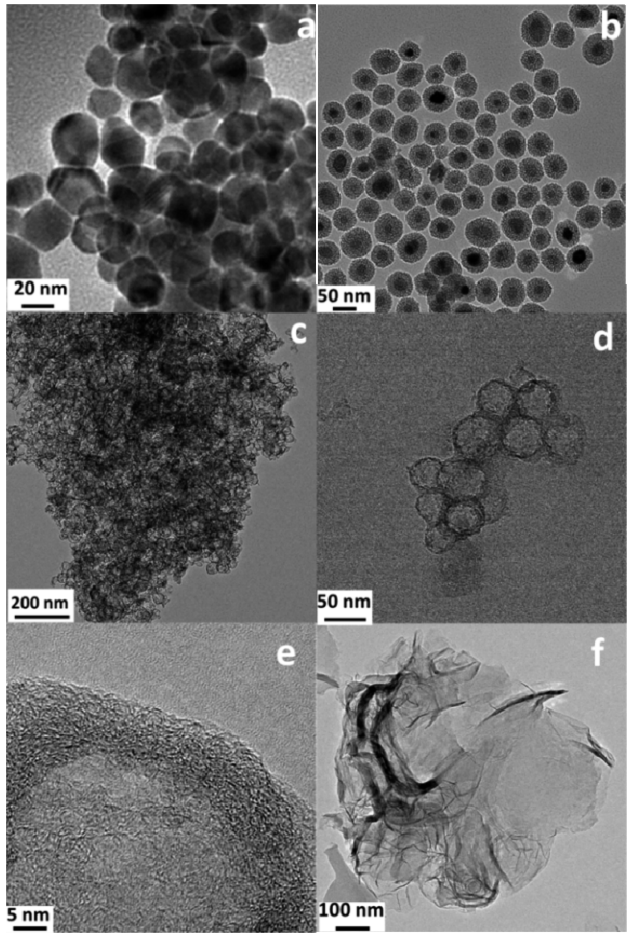

Figure 1. TEM and HRTEM images of (a) CdS nanoparticles, (b) CdS@mSiO$_2$ core–shell nanoparticles, (c–e) carbon nanoshell after pyrolyzation at 900 °C and HF etching, and (f) carbon sheet pyrolyzed at 900 °C and HF etched.

etching off of the hard templates, monodisperse mesoporous carbon nanoshells with a thickness about 10 nm (Figure 1e) are successfully obtained. The diameters of such nanoshells are less than 50 nm (Figure 1c–e), and these are consistent with the sizes of the core–shell templates. Monodisperse carbon nanoshells with a particle size less than 100 nm are scarcely reported.[4,24,25]

The synthesized carbon nanoshells show a BET surface area of 1189 $m^2\ g^{-1}$. The hysteresis loop in Figure 2 indicates the microporous and mesoporous nature of the materials. The pore size distribution of the carbon nanoshells is centered around 0.5 nm in micropore range and around 3.0 and 40 nm in mesopore range (Figure S5) according to the BJH and HK models (Figure 2). The hollow, hierarchical porosity and small size carbon nanoshells all contribute to a large surface area which could help the transportation and adsorption of the reactant O_2. The carbon nanoshells also exhibit high CO_2 uptakes of 105 and 70 cm^3/g at 273 and 298 K, respectively (Figure S6). The high CO_2 uptake values of carbon nanoshells are among the highest level of reported N-decorated carbons and larger than those of well-known zeolitic imidazolate frameworks and MIL-53 (Al) under the same conditions.[10,26–28] This high CO_2 uptake could be partially attributed to the N-doping in the carbon nanoshells that can act as basic centers for attracting acidic CO_2 molecules.[10]

DOI: 10.1021/acscatal.5b00530
ACS Catal. 2015, 5, 3887–3893

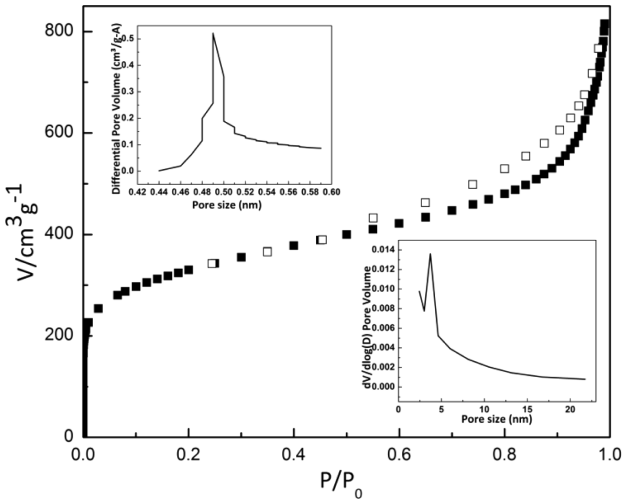

Figure 2. Nitrogen adsorption/desorption isotherms and the corresponding pore size distribution curves for carbon nanoshells pyrolyzed at 900 °C and HF etched.

EDX analysis on carbon nanoshells confirms the presence of carbon, nitrogen and iron (Figure S3). It is considered that metal species stabilized by nitrogen coordination can be durable and positive for oxygen reduction reaction activity although the exact mechanism remains unknown.[8,11,29,30] No metal-containing nanoparticles are observed in TEM and EDX data. By XRD, no crystalline metals or metal oxides can be observed.

The surface Fe, N contents are also confirmed by XPS. The survey scan in Figure S4a reveals the successful introduction of nitrogen and iron atoms into carbon nanoshells after pyrolysis. The contents of nitrogen and iron in the carbon nanoshells are estimated to be 3.71 at% N and 0.34 at% Fe (Table S2). The high resolution N 1s spectra of carbon nanoshells demonstrate the presence of pyridinic, metal-coordinated and graphitic N fitting three different binding energies of 398.3, 399.6, and 401.2 eV, respectively (Figure 3).[31] It is believed that Fe−N*x*,

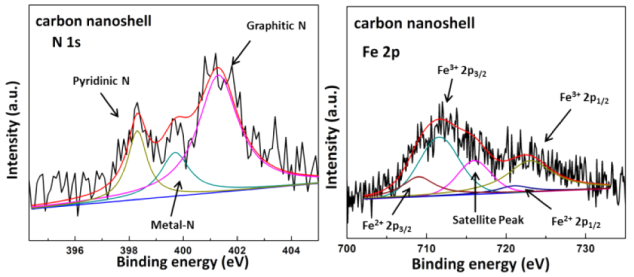

Figure 3. High-resolution N 1s and Fe 2p XPS spectra of carbon nanoshell pyrolyzed at 900 °C and HF etched.

pyridinic N, and graphitic N could all make positive contributions to the ORR activity and durability.[11,32,33] Figure 3 shows the high-resolution Fe 2p spectra. The peaks at 709.2 and 711.9 eV can be assigned to Fe^{2+} and Fe^{3+} species 2p3/2 orbitals binding energies. For the 2p1/2 band, the peak at 721.2 eV is attributed to the binding energy of Fe^{2+} and 723.3 eV for Fe^{3+}. The binding energies of the Fe 2p (around 711 eV) could be ascribed to the N-coordinated Fe^{3+} or Fe^{2+}.[33,34] In addition, both the EDX and XPS results show that after pyrolysis and etching with HF, the carbon nanoshells show no Cadmium left.

For comparison, 4,4′-bipyridine and $FeCl_3{\cdot}6H_2O$ without $CdS@mSiO_2$ core−shell templates are also prepared under similar conditions. After impregnation, pyrolysis and etching with HF, these materials show randomly distributed large carbon sheets in TEM (Figure 1f) (called carbon sheets in the following). The carbon sheets show much lower BET surface area (262 m^2/g) (Figure S5, Table S3). Powder X-ray diffraction (XRD) patterns (Figure S2d) indicate that the synthesized carbon sheets are graphitic carbon with the (002) and (100) planes but with a higher crystallinity; sharp diffraction peaks appear at 26.1 and 43.2 in XRD. However, the higher crystallinity in carbon sheets results in lower nitrogen content as can be seen in the XPS surface content analysis and elemental analysis (Tables S1 and S2). The pyrolysis of 4,4′-bipyridine and $FeCl_3{\cdot}6H_2O$ without template could lead to the easy loss of nitrogen and iron species.

3.2. Catalytic Activity Evaluation. The ORR activity and kinetics of the obtained catalysts is evaluated using ring-disk electrode (RDE) technique at a catalyst loading of 0.1 mg cm^{-2} in 0.1 M KOH and 0.6 mg cm^{-2} in 0.1 M $HClO_4$ at room temperature. The effect of $FeCl_3{\cdot}6H_2O$ and 4,4′-bipyridine ratios on the catalyst activity for ORR is also studied. We find that a ratio of 1:1 is optimal (Figure 4a and b) as revealed by the onset and half-wave potentials in the ORR polarization plots. Therefore, this ratio is used in this project. Calcination temperature also plays an important role in the ORR activity of the produced materials.[33] The best ORR activity of the hollow carbon nanoshells is achieved at 900 °C (Figure 4c and d). Therefore, the catalysts discussed below are all produced at 900 °C.

The steady-state ORR polarization curves in 0.1 M KOH indicate that the carbon nanoshells exhibit an ORR onset potential of 0.98 V vs reversible hydrogen electrode (RHE) determined from a RDE polarization curves at a rotation rate of 1600 rpm (Figure 5a). This is similar to that of Pt/C catalyst (20 μg cm^{-2} Pt) at the same catalyst loading (0.1 mg cm^{-2}). The half-wave potential obtained on the carbon-nanoshell is 0.85 V at 1600 rpm (Figure 5a). Additionally, the carbon-nanoshell shows a higher limiting current density of 5.1 mA cm^{-2} at 0.3 V in alkaline condition, which is larger than that of Pt/C. Figure 5g shows the cyclic voltammograms (CVs) of the carbon nanoshell in Ar and O_2 saturated 0.1 M KOH. Though the CVs for the nanoshell show nearly rectangular shapes in Ar and a well-defined reduction peak at 0.86 V in the O_2 saturated solution which are comparable to that of Pt/C, nanoshells are distinguished by a high peak current of 1.1 mA cm^{-2}.

The electrochemical catalytic activities of carbon nanoshell for ORR in acidic media (0.1 M $HClO_4$) are also studied at a catalyst loading of 0.6 mg cm^{-2}. The polarization curves in 0.1 M $HClO_4$ are displayed in Figure 5b, with the onset potential and the half-wave potential only 30 and 20 mV more negative than those of Pt/C. The decrease of the current density at the potential about 0.7 V in acidic condition may be attributed to the full integration between catalyst and oxygen causing the rapid depletion of the latter. Additionally, the carbon nanoshell shows a limiting current density of 5.4 mA cm^{-2} at 0.3 V acidic conditions, higher than that of Pt/C. In the acidic cyclic voltammograms (CVs) curves, the reduction peak potential of carbon-nanoshell is 0.72 V, only 88 mV smaller than that of Pt/C and with a higher peak current of 2.4 mA cm^{-2}, highlighting the pronounced electrocatalytic activity of carbon nanoshells for oxygen reduction in acidic conditions (Figure 5h).

DOI: 10.1021/acscatal.5b00530
ACS Catal. 2015, 5, 3887−3893

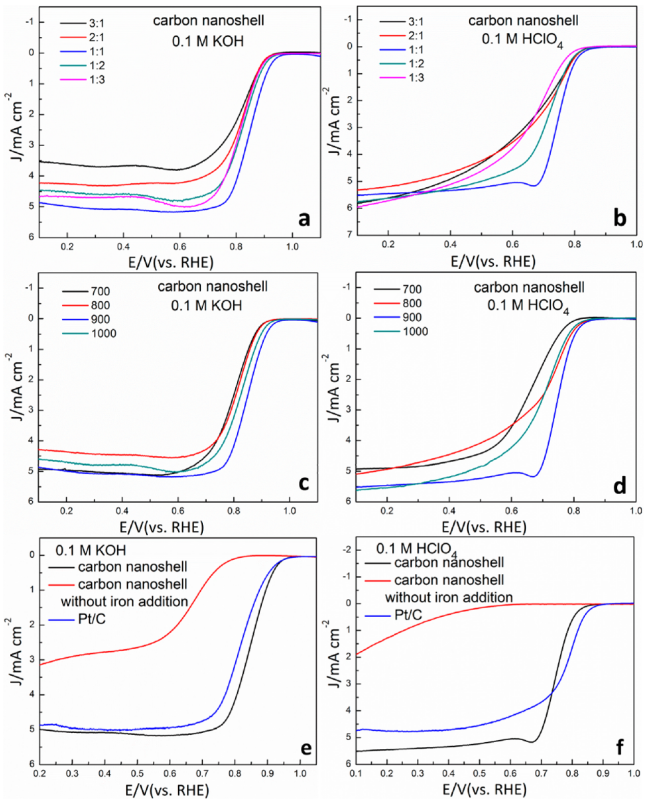

Figure 4. RDE voltammograms of carbon-nanoshell catalysts pyrolyzed by heating the mixtures containing different molar ratios of $FeCl_3 \cdot 6H_2O$ and 4,4′-bipyridine at 900 °C and HF etching in O_2-saturated 0.1 M KOH (a) and 0.1 M $HClO_4$ (b). RDE voltammograms of carbon nanoshells pyrolyzed at different temperatures in O_2-saturated 0.1 M KOH (c) and 0.1 M $HClO_4$ (d). RDE voltammograms of carbon nanoshells, carbon nanoshells without iron addition pyrolyzed at 900 °C and HF etching, and Pt/C in O_2-saturated 0.1 M KOH (e) and in O_2-saturated 0.1 M $HClO_4$ (f). For all tests, the catalyst loading is 0.1 mg cm^{-2} and the scan rate is 10 mV s^{-1} in O_2-saturated 0.1 M KOH. The catalyst loading is 0.6 mg cm^{-2} and the scan rate is 10 mV s^{-1} in O_2-saturated 0.1 M $HClO_4$.

To the best of our knowledge, the values of onset and half wave potentials of the carbon nanoshells in both alkaline and acid conditions are among the best in NPMCs reported to date.[8,35,36] It is worth noting that the onset and half wave potential for the carbon sheets significantly shifted to a more negative potential and lower limiting current density (Figure 5a and b) in both alkaline and acid conditions. This sharp contrast implies the hierarchically porous hollow carbon shell design provides larger surface area and consequently more active sites, facilitating oxygen and electrons transport and diffusion.

In addition, to investigate how the iron affects the electrochemical properties of carbon nanoshells, a controlled experiment is conducted under the same conditions to produce carbon nanoshells but without $FeCl_3 \cdot 6H_2O$ in the preparation. As a result, the polarization curves, the onset and half wave potentials of the obtained material shift negatively in comparison with the prepared carbon nanoshells with iron (Figure 4e and f). The result indicates that the Fe−N*x* active sites indeed contributed to the electroactivity in the obtained carbon nanoshells, though more systematic study is needed to verify the mechanism of active sites in the carbon-nanoshells materials.[8,37]

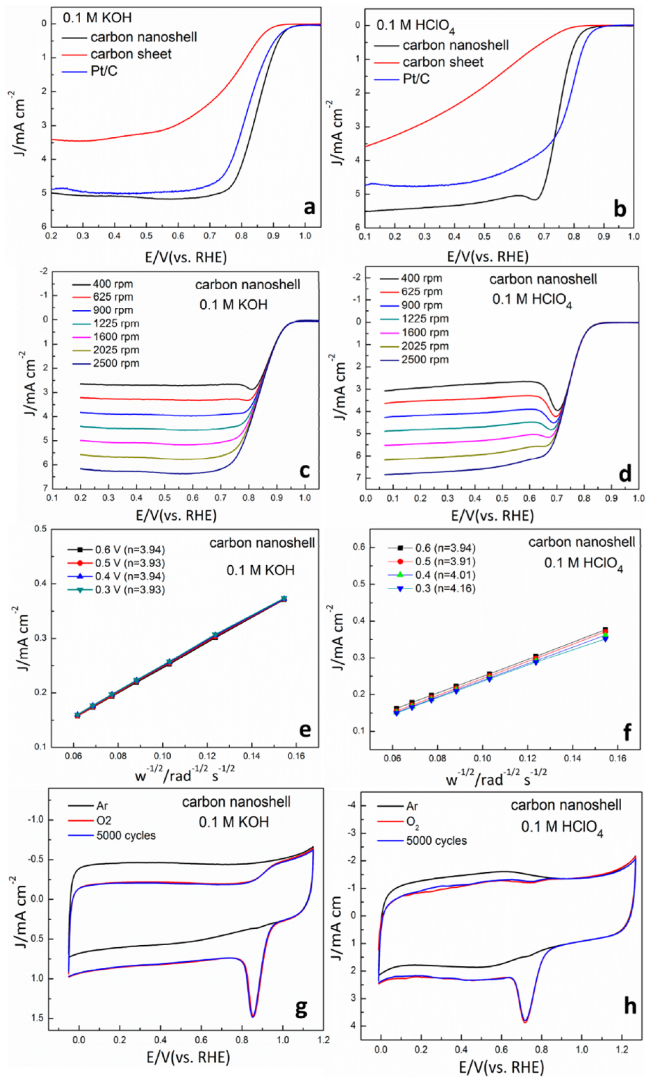

Figure 5. RDE voltammograms of carbon nanoshells, carbon sheet pyrolyzed at 900 °C, HF etched and Pt/C in O_2-saturated 0.1 M KOH (a) and in O_2-saturated 0.1 M $HClO_4$ (b). RDE voltammograms at different rotation rates and Koutecky−Levich plots of carbon nanoshell in O_2-saturated 0.1 M KOH (c, e) and in O_2-saturated 0.1 M $HClO_4$ (d, f). Cyclic voltammograms of carbon nanoshells pyrolyzed at 900 °C and HF etching in O_2-saturated 0.1 M KOH (g) and 0.1 M $HClO_4$ (h). For all tests, the catalyst loading is 0.1 mg cm^{-2} and the scan rate is 10 mV s^{-1} in O_2-saturated 0.1 M KOH. The catalyst loading is 0.6 mg cm^{-2} and the scan rate is 10 mV s^{-1} in O_2-saturated 0.1 M $HClO_4$.

The selectivity of oxygen for the synthesized carbon nanoshells is depicted in linear Koutecky−Levich (KL) plots obtained from the polarization curves at various rotating speeds (Figure 5e and f). The linear sweep voltammetry (LSV) of carbon nanoshells measured with an RDE at various rotating speeds (Figure 5c and d) shows an increasing cathodic current with increasing rotating speed because of the improved mass transport at the electrode surface. The electron transfer number is calculated from the slope of the KL plots to be about 4 at 0.30−0.60 V in alkali and acidic conditions, suggesting that the four-electron reduction pathway to produce water as the main product is favored, a promising characteristic for fuel cell application.

DOI: 10.1021/acscatal.5b00530
ACS Catal. 2015, 5, 3887−3893

In addition, the material also shows good stability. The carbon nanoshells show a stable current−time (i−t) chronoamperometric response after the introduction of 3.0 M methanol in both alkaline and acidic conditions (Figure S7a and b). No noticeable changes are observed in the peak current or capacitive current for the carbon nanoshells in the corresponding cyclic voltammograms for 5000 cycles in 0.1 M KOH and 0.1 $HClO_4$ solutions (Figure 5g and h). Moreover, the carbon nanoshells are also subjected to a chronoamperometric durability test around 50 000 s at ∼0.55 V (vs RHE) in alkaline and acidic condition. As shown in Figure S7c and d carbon nanoshells exhibit a slow attenuation with ∼93% and 95% of the relative current persisted in alkaline and acidic conditions, respectively.

4. CONCLUSIONS

In summary, we report a monodisperse hollow carbon-nanoshells material with highly efficient ORR performance by employing CdS@mSiO_2 core−shell nanoparticles as templates and $FeCl_3 \cdot 6H_2O$ and 4,4′-bipyridine as iron and nitrogen precursors. In respect to the commercial Pt/C catalysts, carbon-nanoshell materials demonstrate excellent ORR activity, high selectivity (direct 4e$^-$ reduction of oxygen to water), superior electrochemical stability and methanol tolerance in both alkaline and acidic conditions. The use of such coordination material may have led to a more uniform distribution of Fe−Nx active sites on the catalyst surface and promote graphitization during heat treatment. Such active sites may also be more accessible with the observed larger surface area and hollow shell design. The hierarchical pore sizes also facilitate mass transport. In addition, we proposed the major active sites as the Fe−Nx species in the carbon nanoshells. Such hollow carbon nanoshells can not only serve as high-performance electrocatalysts for ORR but also offer a new synthesis route to prepare efficient electrode materials.

■ ASSOCIATED CONTENT

Supporting Information

The Supporting Information is available free of charge on the ACS Publications website at DOI: 10.1021/acscatal.5b00530.

Structure, textural properties, and electrochemical measurement results for carbon nanoshells and carbon sheets materials (PDF)

■ AUTHOR INFORMATION

Corresponding Author

*E-mail: pingyun.feng@ucr.edu.

Notes

The authors declare no competing financial interest.

■ ACKNOWLEDGMENTS

This work is supported by the U.S. Department of Energy, Office of Basic Energy Sciences, Division of Materials Sciences and Engineering under Award no. DE-FG02-13ER46972 (P.F.).

■ REFERENCES

(1) Borup, R.; Meyers, J.; Pivovar, B.; Kim, Y. S.; Mukundan, R.; Garland, N.; Myers, D.; Wilson, M.; Garzon, F.; Wood, D.; Zelenay, P.; More, K.; Stroh, K.; Zawodzinski, T.; Boncella, J.; McGrath, J. E.; Inaba, M.; Miyatake, K.; Hori, M.; Ota, K.; Ogumi, Z.; Miyata, S.; Nishikata, A.; Siroma, Z.; Uchimoto, Y.; Yasuda, K.; Kimijima, K.-i.; Iwashita, N. *Chem. Rev.* **2007**, *107*, 3904−3951.
(2) Gong, K.; Du, F.; Xia, Z.; Durstock, M.; Dai, L. *Science* **2009**, *323*, 760−764.
(3) Li, Y.; Zhou, W.; Wang, H.; Xie, L.; Liang, Y.; Wei, F.; Idrobo, J.-C.; Pennycook, S. J.; Dai, H. *Nat. Nanotechnol.* **2012**, *7*, 394−400.
(4) Li, Q.; Cao, R.; Cho, J.; Wu, G. *Adv. Energy Mater.* **2014**, *4*, 1301415.
(5) Wu, G.; More, K. L.; Johnston, C. M.; Zelenay, P. *Science* **2011**, *332*, 443−447.
(6) Kong, A.; Zhu, X.; Han, Z.; Yu, Y.; Zhang, Y.; Dong, B.; Shan, Y. *ACS Catal.* **2014**, *4*, 1793−1800.
(7) Zhang, L.; Kim, J.; Dy, E.; Ban, S.; Tsay, K.-c.; Kawai, H.; Shi, Z.; Zhang, J. *Electrochim. Acta* **2013**, *108*, 814−819.
(8) Lin, L.; Zhu, Q.; Xu, A. W. *J. Am. Chem. Soc.* **2014**, *136*, 11027−11033.
(9) Lee, J.-S.; Park, G. S.; Kim, S. T.; Liu, M.; Cho, J. *Angew. Chem., Int. Ed.* **2013**, *52*, 1026−1030.
(10) Aijaz, A.; Fujiwara, N.; Xu, Q. *J. Am. Chem. Soc.* **2014**, *136*, 6790−6793.
(11) Liang, H.-W.; Wei, W.; Wu, Z.-S.; Feng, X.; Muellen, K. *J. Am. Chem. Soc.* **2013**, *135*, 16002−16005.
(12) Ito, Y.; Qiu, H. J.; Fujita, T.; Tanabe, Y.; Tanigaki, K.; Chen, M. *Adv. Mater.* **2014**, *26*, 4145−4150.
(13) Han, C. L.; Wang, S. P.; Wang, J.; Li, M. M.; Deng, J.; Li, H. R.; Wang, Y. *Nano Res.* **2014**, *7*, 1809−1819.
(14) Zhou, M.; Yang, C. Z.; Chan, K. Y. *Adv. Energy Mater.* **2014**, DOI: 10.1002/aenm.201400840.
(15) Sanetuntikul, J.; Hang, T.; Shanmugam, S. *Chem. Commun.* **2014**, *50*, 9473−9476.
(16) Wang, H.; Bo, X.; Wang, A.; Guo, L. *Electrochem. Commun.* **2013**, *36*, 75−79.
(17) Yu, Y. M.; Zhang, J. H.; Xiao, C. H.; Zhong, J. D.; Zhang, X. H.; Chen, J. H. *Fuel Cells* **2012**, *12*, 506−510.
(18) Schaefer, Z. L.; Gross, M. L.; Hickner, M. A.; Schaak, R. E. *Angew. Chem., Int. Ed.* **2010**, *49*, 7045−7048.
(19) Li, N.; Zhang, X.; Chen, S.; Hou, X. *J. Phys. Chem. Solids* **2011**, *72*, 1195−1198.
(20) Kim, J.; Kim, H. S.; Lee, N.; Kim, T.; Kim, H.; Yu, T.; Song, I. C.; Moon, W. K.; Hyeon, T. *Angew. Chem., Int. Ed.* **2008**, *47*, 8438−8441.
(21) Ruggeri, S.; Dodelet, J.-P. *J. Electrochem. Soc.* **2007**, *154*, B761−B769.
(22) Charreteur, F.; Jaouen, F.; Ruggeri, S.; Dodelet, J.-P. *Electrochim. Acta* **2008**, *53*, 2925−2938.
(23) Wen, Z.; Ci, S.; Hou, Y.; Chen, J. *Angew. Chem., Int. Ed.* **2014**, *53*, 6496−6500.
(24) Wu, G.; Zelenay, P. *Acc. Chem. Res.* **2013**, *46*, 1878−1889.
(25) Guo, S.; Zhang, S.; Sun, S. *Angew. Chem., Int. Ed.* **2013**, *52*, 8526−8544.
(26) Wang, L.; Yang, R. T. *J. Phys. Chem. C* **2012**, *116*, 1099−1106.
(27) Sumida, K.; Rogow, D. L.; Mason, J. A.; McDonald, T. M.; Bloch, E. D.; Herm, Z. R.; Bae, T. H.; Long, J. R. *Chem. Rev.* **2012**, *112*, 724−781.
(28) Phan, A.; Doonan, C. J.; Uribe-Romo, F. J.; Knobler, C. B.; O'Keeffe, M.; Yaghi, O. M. *Acc. Chem. Res.* **2010**, *43*, 58−67.
(29) Ferrandon, M.; Kropf, A. J.; Myers, D. J.; Artyushkova, K.; Kramm, U.; Bogdanoff, P.; Wu, G.; Johnston, C. M.; Zelenay, P. *J. Phys. Chem. C* **2012**, *116*, 16001−16013.
(30) Jaouen, F.; Proietti, E.; Lefevre, M.; Chenitz, R.; Dodelet, J.-P.; Wu, G.; Chung, H. T.; Johnston, C. M.; Zelenay, P. *Energy Environ. Sci.* **2011**, *4*, 114−130.
(31) Kothandaraman, R.; Nallathambi, V.; Artyushkova, K.; Barton, S. C. *Appl. Catal., B* **2009**, *92*, 209−216.
(32) Wu, G.; Johnston, C. M.; Mack, N. H.; Artyushkova, K.; Ferrandon, M.; Nelson, M.; Lezama-Pacheco, J. S.; Conradson, S. D.; More, K. L.; Myers, D. J.; Zelenay, P. *J. Mater. Chem.* **2011**, *21*, 11392−11405.

(33) Zhao, Y.; Watanabe, K.; Hashimoto, K. *J. Am. Chem. Soc.* **2012**, *134*, 19528−19531.
(34) Kong, A.; Kong, Y.; Zhu, X.; Han, Z.; Shan, Y. *Carbon* **2014**, *78*, 49−59.
(35) Hu, Y.; Jensen, J. O.; Zhang, W.; Cleemann, L. N.; Xing, W.; Bjerrum, N. J.; Li, Q. *Angew. Chem., Int. Ed.* **2014**, *53*, 3675−3679.
(36) Hou, Y.; Huang, T.; Wen, Z.; Mao, S.; Cui, S.; Chen, J. *Adv. Energy Mater.* **2014**, DOI: 10.1002/aenm.201400337.
(37) Ramaswamy, N.; Tylus, U.; Jia, Q.; Mukerjee, S. *J. Am. Chem. Soc.* **2013**, *135*, 15443−15449.

DOI: 10.1021/acscatal.5b00530
ACS Catal. 2015, 5, 3887−3893